Large tunability of the magnetoelectric effect in the Co-substituted polar antiferromagnet Ni_3TeO_6

J. H. Zhang,[1] L. Lin,[1,2,*] Y. S. Tang,[1,3] G. Z. Zhou,[1] L. Huang,[1] X. Y. Li,[1] G. Y. Li,[1] S. H. Zheng,[1,4] M. F. Liu,[1,4] X. M. Liu,[5] Z. B. Yan,[1] X. K. Huang,[6] C. Chen,[6] X. P. Jiang,[6] and J.-M. Liu[1]

[1]*Laboratory of Solid State Microstructures and Department of Physics, Nanjing University, Nanjing 210093, China*
[2]*Department of Applied Physics, College of Science, Nanjing Forestry University, Nanjing 210037, China*
[3]*School of Science, Nanjing University of Posts and Telecommunications, Nanjing 210023, China*
[4]*Institute for Advanced Materials, Hubei Normal University, Huangshi 435002, China*
[5]*Institute of Mathematical and Physical Sciences, Jiangsu University of Science and Technology, Zhenjiang 212003, China*
[6]*School of Materials Science and Engineering, Jingdezhen Ceramic Institute, Jingdezhen 333001, China*

(Received 15 January 2023; revised 24 May 2023; accepted 13 July 2023; published 31 July 2023)

Polar magnet Ni_3TeO_6 has been recently attracting considerable interest due to its nonhysteretic magnetoelectricity associated with the collinear antiferromagnetic (AFM) order. Nevertheless, the magnetoelectric (ME) response in Ni_3TeO_6 remains trivial, and especially lacks sufficient tunability. Herein, we report large tunability of the ME effect in Co-substituted Ni_3TeO_6, and special attention is paid to Ni_2CoTeO_6 and $NiCo_2TeO_6$ single crystals where incommensurate AFM helical structure with spins lying in the *ab* plane is established, distinctly different from the collinear AFM structure in Ni_3TeO_6 along the *c* axis. Our results demonstrate that the Co^{2+} substitution results in emergence of a giant electric polarization P_c up to $\sim 0.52\ \mu C/cm^2$ induced by a magnetic field normal to the *c* axis, i.e., the polar axis. The generated P_c in $NiCo_2TeO_6$ is approximately 8.45 and 1.8 times larger than that of Ni_2CoTeO_6 and Ni_3TeO_6, respectively. More importantly, the linear ME coefficient α can be remarkably modulated by the Co^{2+} substitution, evidenced with a large $\alpha \sim 323$ ps/m for $NiCo_2TeO_6$, a small $\alpha \sim 3.4$ ps/m for Ni_2CoTeO_6, and an intermediate $\alpha \sim 36$ ps/m for Ni_3TeO_6 at temperature $T \sim 45$ K. Such remarkable Co-substitution control of the ME effect is believed to be associated with the different occupations of the Ni/Co ions at the specific lattice sites. This work thus provides insights into the high-tunability ME effect in Ni_3TeO_6 polar magnets, a largely unexplored topic.

DOI: 10.1103/PhysRevB.108.024107

I. INTRODUCTION

Multiferroics, where magnetic and ferroelectric orders coexist and couple with each other, has attracted much attention over the past two decades, due to its intriguing physics and promising applications in multifunctional devices [1–5]. However, constrained by the requirement of complex types of magnetic textures, few materials do exhibit large magnetically induced electric polarization (P) and strong magnetoelectric (ME) coupling [6–11]. Therefore, enormous effort has been devoted to designing and searching for new multiferroic materials with strong ME coupling and high magnetic-ordering temperature (T_c) [12–14]. An alternative route to pursue the large ME effect is to consider polar magnets in which space-inversion symmetry and time-reversal symmetry are simultaneously broken. Subsequently, the metamagnetic transitions, e.g., spin flop, magnetic plateau, ferrimagnetic transition, etc. may distort the polar crystal structure to modify the electric polarization. A large ME effect is thus stimulated, accompanied by magnetic transitions via symmetric exchange striction [15,16].

The corundum-related compound Ni_3TeO_6 belongs to such kind of materials that exhibit colossal magnetoelectricity [17]. Ni_3TeO_6 crystalizes in a polar $R3$ structure with Ni2/Ni3-O6 octahedra layer and Ni1-O6 octahedra layer alternating along the *c* axis, as illustrated by VESTA software [18] in Fig. 1(a), where symbols Ni1, Ni2, and Ni3 denote the different Ni occupations. The octahedra are connected through two oxygen ions in each layer, forming a coplanar honeycomb lattice of edge-sharing octahedra, shown in Figs. 1(b) and 1(c). It is known that Ni_3TeO_6 undergoes a collinear antiferromagnetic (AFM) ordering along the *c* axis below its Néel temperature $T_N \sim 52$ K, giving rise to a large and magnetically induced electric polarization up to $0.33\ \mu C/cm^2$ at temperature $T = 2$ K, a giant polarization for multiferroics [17]. In addition, a nonhysteresis colossal ME effect occurs at a critical spin-flop magnetic field $H_c \sim 9$ T, while another new metamagnetic transition with giant ME coupling at $H \sim 52$ T was discovered by high magnetic field measurements [19]. Optical spectroscopy revealed the large change in electric polarization associated with the magnetic field-induced changes in the crystal-field environment of Ni1 and Ni2 sites [20].

Until recently, it was reported that partially substituted Ni^{2+} with other $3d$ transition-metal ions such as Mn^{2+}, Co^{2+}, and Cu^{2+} can preserve the noncentrosymmetric space group $R3$, while the magnetic structure can be flexibly tuned, although the independent parent compounds have different crystal and magnetic structures [21,22]. For example, the AFM Néel point T_N is largely enhanced from ~ 52 to

*llin@njfu.edu.cn

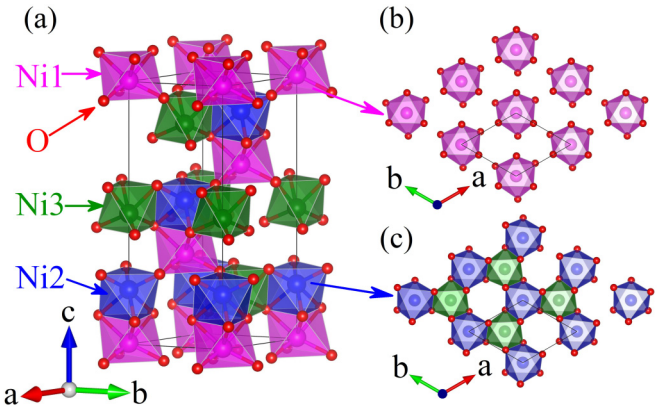

FIG. 1. (a) Crystal structure of Ni_3TeO_6 with Ni ions occupying three distinct sites denoted as Ni1, Ni2, and Ni3, respectively. Here, only Ni^{2+} and O^{2-} ions are shown for simplicity. View as a stack of alternating Ni1/Ni2-O6 and Ni3-O6 layers along crystallographic c axis is presented in (b) and (c), respectively.

$\sim$ 75 K via the Mn substitution, and an incommensurate helical magnetic phase with the spins lying in the *ab* plane emerges between $T_N \sim 75$ K and $T \sim 65$ K, below which a collinear commensurate AFM ordering along the c axis, identical to Ni_3TeO_6, was observed [21]. Unfortunately, it seems that the ME performance is seriously destroyed, leaving a big challenge to the effort of keeping high operating temperature and large ME effect simultaneously. This issue becomes somehow different for the case of Co^{2+}-substitution of Ni^{2+}, since the reported two compounds, Ni_2CoTeO_6 and $NiCo_2TeO_6$, both order into incommensurate AFM helical state, in which the spins are aligned in the *ab* plane and the magnetic propagation vector $k = (0,\ 0,\ 1.2994)$ and $k = (0,\ 0,\ 1.2091)$, respectively [22]. These facts are in contrast to the collinear magnetic structure in Ni_3TeO_6 [17] and complex magnetic ordering in Co_3TeO_6 [23]. Furthermore, the ME effect in Co_3TeO_6 is also somehow suppressed but a nonzero magnetically induced electric polarization (up to 24 $\mu C/m^2$ at $T \sim 5$ K and $H \sim 9$ T) still survives [24]. It is thus suggested that the Co substitution in Ni_3TeO_6 may play a different role with respect to the cases of Mn^{2+} substitution of Ni^{2+}. For the Cu-doping case, the solubility limit of Cu in Ni_3TeO_6, prepared by the solid-state reaction method, is slightly below $x = 0.5$, above which the sample shows phase separation or precipitation [25]. Unfortunately, the effect of Cu doping on the magnetic and ME behaviors of Ni_3TeO_6 is still unknown so far and worthy of further investigation.

In this regard, it is now understood that a proper chemical substitution in Ni_3TeO_6 could be an effective approach to improve the ME response and multiferroic behaviors. It is known that the chemical substitution usually contributes to a modulation of magnetic structure and ME coupling. Bearing in mind that the colossal magnetoelectricity is most likely associated with the collinear spin order, the incommensurate helical magnetic phase seems not to benefit the ME coupling, considering the Mn^{2+}-substitution case. Because large anisotropy, strong spin-orbit coupling, and large magnetostriction are typically found in cobaltites [14], it would be of particular interest to check how the ME effect evolves when an incommensurate AFM helical structure driven by Co^{2+} substitution is introduced. However, so far no systematic investigation of the ME coupling in Co-substituted Ni_3TeO_6 has yet been reported, probably due to the limited size of the as-grown crystals [22].

Motivated by these discussions, we have successfully grown sufficiently large slices of Co-substituted Ni_3TeO_6 single crystals $Ni_{3-x}Co_xTeO_6$ ($x = 1,\ 2$), making the ME effect measurements accessible. We find a distinct substitution-induced ME modulation in polar magnet Ni_3TeO_6, whereas the magnetic phase could be tuned by optimizing the Co^{2+}-Ni^{2+} interaction, as previously revealed in Zn-doped $MnWO_4$ [26], $Fe_2Mo_3O_8$ [27], Ga- and Al-doped $CuFeO_2$ [28], Sc-doped $BaFe_{12}O_{19}$ [29], etc. Upon the Co^{2+} substitution, a metamagnetic transition occurs at critical magnetic field $H_c \sim 7.5$ and 2.0 T for $x = 1$ and $x = 2$, respectively, when the magnetic field is applied along the *ab* plane. Accompanied by the metamagnetic transition, a large electric polarization is observed. More interestingly, in comparison with the parent compound Ni_3TeO_6, $Ni_{3-x}Co_xTeO_6$ ($x = 1,\ 2$) shows a large difference in terms of the ME performance. For the case of $x = 1$, the ME response is largely diluted, while remarkable enhancement for the case of $x = 2$ is demonstrated, evidenced by an ME response as large as 326 ps/m in terms of the linear ME coefficient (α) at $T \sim 45$ K above H_c, almost 9 times large than that of parent compound Ni_3TeO_6.

II. EXPERIMENTAL DETAILS

Polycrystalline $Ni_{3-x}Co_xTeO_6$ ($x = 0,\ 1,\ 2$) was prepared by the conventional solid-state reaction method [22]. A stoichiometric amount of high-purity NiO, TeO_2, and CoO was mixed, ground, and sintered in a tubular furnace under the oxygen flux at 800 °C with several intermediate grindings to ensure a complete reaction. The chemical vapor transport method was used to grow single crystals from the obtained polycrystalline powder. In detail, the polycrystalline powder with a total mass of 3 g as the starting material was placed in a quartz tube (inner diameter = 20 mm, outer diameter = 22 mm, and length = 20 cm), and sealed under the vacuum of 10^{-4} Torr. Then, the tube was placed in a horizontal two-zone furnace, and heated at 830 °C in the change zone and 750 °C in the growth zone for 2 weeks, followed by furnace cooling, noting that the starting materials were placed in the warmer zone.

The as-grown Ni_2CoTeO_6 and $NiCo_2TeO_6$ crystals are naturally black hexagonal plates with a typical size up to 4 mm, while the Ni_3TeO_6 crystals are triangle-like plates with size up to 3 mm. The crystallinity of as-grown single crystals was characterized using room-temperature powder x-ray diffraction (XRD) (D8 ADVANCE, Bruker) with Cu K_α ($\lambda = 1.5406$ Å). Crystallographic orientation was determined using the backreflection Laue detector (MWL120, Multiwire Laboratories, Ltd.). The chemical composition was determined using scanning electron microscopy with an energy-dispersive x-ray spectroscopy (EDX) unit. The Rietveld refinement of the lattice structure and species occupation was performed using the GSAS program [30].

The well-prepared and aligned samples were submitted for a series of structural and physical property characterizations.

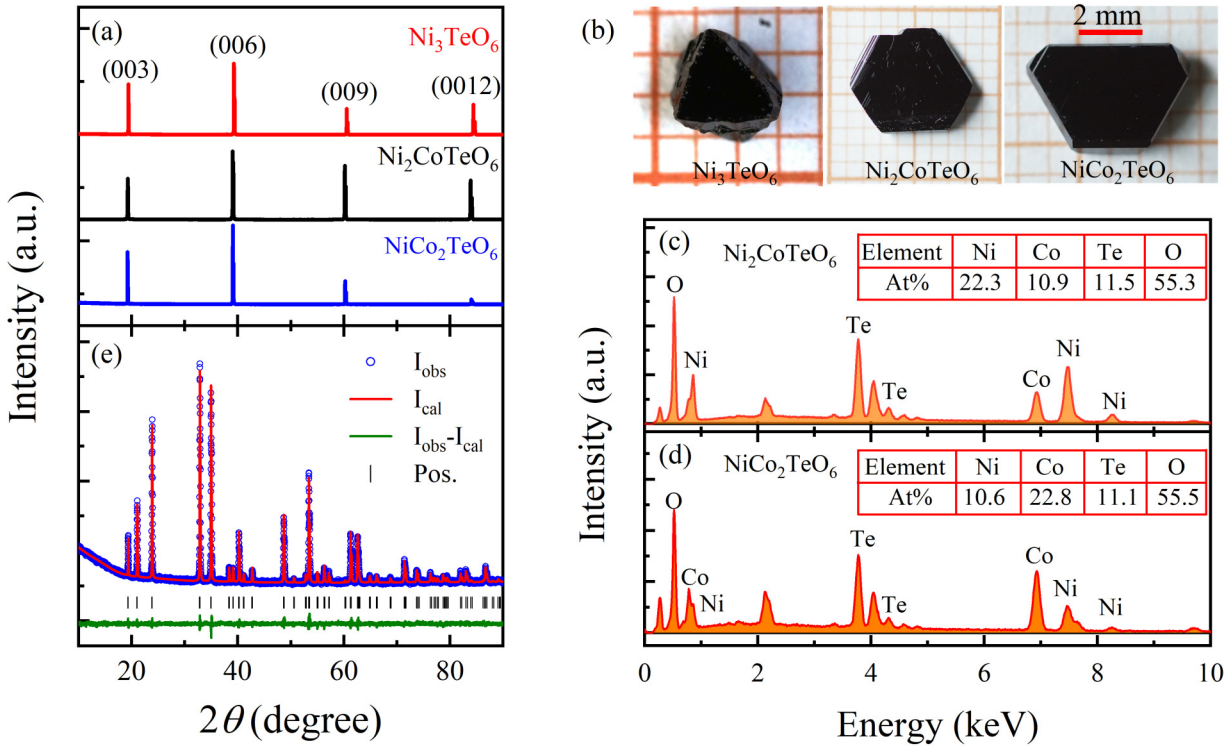

FIG. 2. (a) Room temperature XRD patterns of Ni_3TeO_6, Ni_2CoTeO_6, and $NiCo_2TeO_6$ single crystals. (b) Optical photograph of Ni_3TeO_6, Ni_2CoTeO_6, and $NiCo_2TeO_6$ single crystals. EDX spectrum of (c) Ni_2CoTeO_6 and (d) $NiCo_2TeO_6$. (e) Room temperature XRD pattern and Rietveld refinement of crushed single crystal of $NiCo_2TeO_6$.

The dc magnetic susceptibility (χ) as a function of T was measured using the Quantum Design superconducting quantum interference device magnetometer with a measuring magnetic field $H \sim 0.1$ T in the zero-field-cooled (ZFC) and field-cooled (FC) modes. The H-dependent magnetization (M) was measured using the vibrating sample magnetometer in the Physical Property Measurement System (PPMS, Quantum Design).

For the electrical measurement, the crystals were polished into slices of $3 \times 3 \times 0.2$ mm^3 and deposited with Au electrodes on the top and bottom surfaces. The electric polarization was obtained by conventional pyroelectric current measurements. In detail, the sample was poled under an electric field $E_{pole} = 10$ kV/cm and selected magnetic field (H) from $T = 70$ to 2 K. Then, the poling electric field was removed and the sample was electrically short-circuited for sufficient time to avoid the influence of injected charge. The T dependence of pyroelectric current (J) at selected H was measured using a Keithley 6514 source meter at the 3 K/min warming rate. The H dependence of ME current was measured under selected T upon H ramping from $+H \rightarrow -H \rightarrow +H$ at a rate of 100 Oe/s using the same ME poling procedure. The H- and T-dependent electric polarization P was obtained by integrating pyroelectric current/magnetoelectric current with time, following the well-established procedure [31].

III. RESULTS AND DISCUSSION

A. Crystal structure

In Fig. 2(a) we present the room-temperature slow-scan XRD patterns onto the naturally developed c planes of Ni_3TeO_6, Ni_2CoTeO_6, and $NiCo_2TeO_6$ crystals, in which the diffraction peaks can be well indexed by ($00l$) reflections. Compared with the previously reported crystal growth [17,21], our crystals have more regular geometric shape and larger lateral dimension, as shown in Fig. 2(b), quite advantageous for the electrical measurements. In addition, the c plane is aligned with the backreflection Laue detector, and perfect diffraction spots from the [$00l$] reflections are unambiguously identified without any additional spots (the Laue diffraction spots and Rietveld refinement of Ni_3TeO_6 are included in the Supplemental Material; see Fig. S1) [32]. Furthermore, as shown in Figs. 2(c) and 2(d), the measured Ni:Co:Te ratio for these single crystals grown from polycrystalline Ni_2CoTeO_6 and $NiCo_2TeO_6$ powder is 1.96:0.94:1 and 0.95:2.05:1, respectively, close to the stoichiometric ratio of Ni_2CoTeO_6 and $NiCo_2TeO_6$. The corresponding EDX mapping images of Ni_2CoTeO_6 and $NiCo_2TeO_6$ are also presented in Figs. S2 and S3 in the Supplemental Material [32].

To check the solubility of Co in Ni_3TeO_6, a series of polycrystalline $Ni_{3-x}Co_xTeO_6$ samples were synthesized by the conventional solid-state reaction method, and the XRD patterns are shown in Fig. S4 [32]. It is evident that the samples with Co doping level $x \leqslant 2.6$ adopt the structural model of Ni_3TeO_6, while we found additional diffraction peaks of monoclinic Co_3TeO_6 upon further increasing x beyond 2.6. Therefore, the solubility limit of Co in Ni_3TeO_6 is most likely below or near $x = 2.6$. We then determined the crystal structure from the crushed single crystals of $NiCo_2TeO_6$ at room temperature, using Rietveld refinement with powder XRD, as shown in Fig. 2(e). All the diffraction peaks were well indexed using the space group $R3$ and no impurity phase

TABLE I. Crystal structural parameters of Ni_3TeO_6 (NTO), Ni_2CoTeO_6 (NC1), and $NiCo_2TeO_6$ (NC2) refined from XRD of crushed crystal data at room temperature.

Sample	a (Å)	b (Å)	c (Å)	α (°)	β (°)	γ (°)
NTO	5.1128(8)	5.1128(8)	13.7806(8)	90	90	120
NC1	5.1385(4)	5.1385(4)	13.8253(2)	90	90	120
NC2	5.1653(8)	5.1653(8)	13.8482(5)	90	90	120
	Atom	x	y	z	Wyckoff	occupation
	Ni3	1/3	2/3	0.1660(7)	3*a*	1.015
	Ni2	1.0000	1.0000	0.2099(4)	3*a*	1.006
NTO	Ni1	2/3	1/3	0.3392(2)	3*a*	1.031
	Te	1/3	2/3	0.3673(3)	3*a*	0.998
	O1	0.6296(8)	0.6610(4)	0.2774(8)	9*b*	0.983
	O2	0.9871(3)	0.6292(4)	0.4396(7)	9*b*	0.985
	Ni3/Co3	1/3	2/3	0.1791(8)	3*a*	0.753/0.247
	Ni2/Co2	1.0000	1.0000	0.2249(7)	3*a*	0.453/0.547
	Ni1/Co1	2/3	1/3	0.3529(1)	3*a*	0.776/0.224
NC1	Te	1/3	2/3	0.3816(7)	3*a*	0.996
	O1	0.6268(1)	0.6441(2)	0.2867(4)	9b	1.027
	O2	0.9875(1)	0.6101(2)	0.4500(7)	9b	0.973
	Ni3/Co3	1/3	2/3	0.1711(6)	3*a*	0.535/0.465
	Ni2/Co2	1.000000	1.000000	0.2043(5)	3*a*	0/1
NC2	Ni1/Co1	2/3	1/3	0.3444(3)	3*a*	0.475/0.525
	Te	1/3	2/3	0.3807(2)	3*a*	0.984
	O1	0.6303(1)	0.6519 (8)	0.2825(6)	9*b*	0.976
	O2	0.9910(4)	0.6263(4)	0.4476(9)	9*b*	0.992
	R_p (%)		R_{wp} (%)		χ^2	
NTO	3.59		5.23		1.812	
NC1	2.48		3.38		1.39	
NC2	2.34		3.26		1.53	

was detected. The corresponding lattice parameters were $a = 5.1653$ Å and $c = 13.8482$ Å, in good agreement with earlier results [22]. Detailed refined structural parameters of Ni_3TeO_6, Ni_2CoTeO_6, and $NiCo_2TeO_6$ are summarized in Table I.

The structural Rietveld refinement suggests that for Ni_2CoTeO_6 ($x = 1$), the Co^{2+} ions partially substitute the Ni ions in the Ni1, Ni2, and Ni3 sites, but more favorable substitution is believed to occur at the Ni2 site. In contrast, for $NiCo_2TeO_6$ ($x = 2$), the Ni2 sites are almost fully occupied by Co^{2+} ions, while the Ni1 and Ni3 sites are partially substituted with Co^{2+} ions with nearly equal occupancy, similar to previously reported results on $Ni_{2.1}Mn_{0.9}TeO_6$ [21]. Such preferential site occupancy of Co ions in various Ni sites may be associated with the different distortions of the three Ni sites, whereas the Ni3 sites have the largest distortion, followed by the Ni1 and Ni2 sites, but the Ni2 site retains the most symmetric C3 symmetry. Therefore, the different site occupancy of Co ions reflects the change in the crystal-field environment of Ni and Co sites, thereby raising an important issue on the evolution of the electric polarization and ME response upon Co^{2+} substitution, which will be discussed later.

B. Magnetic property

Figures 3(a)–3(c) present the T-dependent χ curves measured along the directions parallel and perpendicular to the c axis in the ZFC mode for Ni_3TeO_6, Ni_2CoTeO_6, and $NiCo_2TeO_6$, respectively. The $\chi(T)$ curves show clear long-range AFM ordering at 54 K for Ni_3TeO_6, 54 K for Ni_2CoTeO_6, and 49 K for $NiCo_2TeO_6$, slightly lower than previously reported values, e.g., 55 and 52 K for Ni_2CoTeO_6 and $NiCo_2TeO_6$, respectively [22]. Furthermore, compared with Ni_3TeO_6, several interesting features deserve highlighting. First, upon cooling from T_N, for Ni_3TeO_6, the measured χ_c, i.e., the out-of-plane χ, suddenly decreases while the measured χ_{ab}, the in-plane χ, exhibits a relative weak T dependence, where subscripts "*ab*" and "*c*" denote the *ab* plane and *c* axis. In Ni_2CoTeO_6 and $NiCo_2TeO_6$, the situation is opposite: χ_{ab} suddenly decreases while χ_c exhibits a weak T dependence, indicating that the magnetic moments in Ni_2CoTeO_6 and $NiCo_2TeO_6$ are aligned perpendicularly to the *c* axis, in accordance with the magnetic structure data [22]. Second, the in-plane and out-of-plane $\chi(T)$ curves exhibit a large difference for both Ni_2CoTeO_6 and $NiCo_2TeO_6$, especially for $NiCo_2TeO_6$, while little difference for Ni_3TeO_6 is clearly seen, implying a remarkable easy-plane type single-ion anisotropy of Co^{2+} ions in Ni_2CoTeO_6 and $NiCo_2TeO_6$. Third, although Ni_2CoTeO_6 and $NiCo_2TeO_6$ have similar magnetic structures, the magnitude of $\chi_{ab}(T)$ for $NiCo_2TeO_6$ is much larger than that for Ni_2CoTeO_6, indicating that the increasing Co^{2+}-doping level can significantly influence the magnetic property along the *ab* plane.

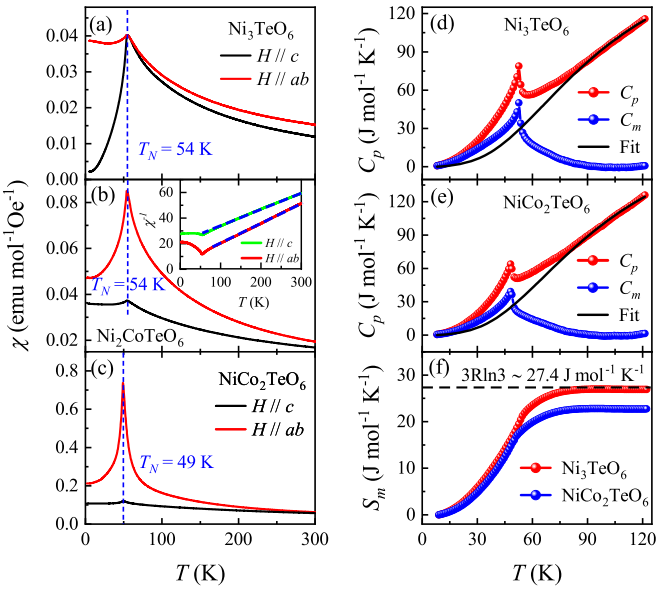

FIG. 3. Temperature dependence of magnetic susceptibility in magnetic field applied along and perpendicular to c axis in ZFC mode for (a) Ni_3TeO_6, (b) Ni_2CoTeO_6, and (c) $NiCo_2TeO_6$. Vertical blue dashed lines indicate magnetic transition points. Inset in (b) shows Curie-Weiss fitting for Ni_2CoTeO_6 under $H//c$ and $H//ab$ geometry. T-dependent specific heat (C_p) for (d) Ni_3TeO_6 and (e) $NiCo_2TeO_6$. Black solid curves are phonon contribution approximated by Debye model. (f) T-dependent magnetic entropy of Ni_3TeO_6 and $NiCo_2TeO_6$.

Fitting the linear part of the inverse magnetic susceptibility χ^{-1} data between 100 and 300 K using the Curie-Weiss law (see Fig. 3, inset), one obtains the Curie-Weiss temperatures $\theta_{CW} \sim -169.6$ and -27.3 K for Ni_2CoTeO_6 under the $H//c$ and $H//ab$ conditions, respectively, indicating the AFM interactions among the Ni^{2+}/Co^{2+} moments. The fitted data reveal that the frustration factor, defined by $f = |\theta_{CW}/T_N|$ along the c axis, is ~ 3.1 for Ni_2CoTeO_6 and ~ 4.2 for $NiCo_2TeO_6$, indicative of the weak frustration in the Co-substituted Ni_3TeO_6 system. The detailed values fitted from the Curie-Weiss law are listed in Table II. The table shows the effective moment μ_{eff} is obviously larger than the calculated value μ_{cal} using the spin-only moments $\mu_{Ni}^{2+} = 2.8\ \mu_B$ and $\mu_{Co}^{2+} = 3.8\ \mu_B$. This indicates the non-negligible contribution of the orbital angular momentum to the effective magnetic moment via the spin-orbit coupling of Co^{2+}, similar to previously reported results on $Co_4Nb_2O_9$ [6].

Figures 3(d) and 3(e) present the T dependences of the heat capacity for Ni_3TeO_6 and $NiCo_2TeO_6$, respectively. The typical λ-shaped peak is seen around the magnetic-ordering temperature $T_N = 54$ K for Ni_3TeO_6 and $T_N = 48$ K for $NiCo_2TeO_6$. Usually, one may extract the magnetic contribution to the heat capacity by referring to a nonmagnetic isostructural system. Unfortunately, it is known that among the transition-metal telluride M_3TeO_6 (M = Mg, Mn, Co, Ni, Zn, Cu) compounds, Mg_3TeO_6 [33] and Mn_3TeO_6 [34] show the centrosymmetric space group R-3, Zn_3TeO_6 [35] and Co_3TeO_6 [36] are centrosymmetric ($C2/c$), and Cu_3TeO_6 belongs to the cubic space group Ia-3 [37]. Only Ni_3TeO_6 [38] crystallizes into polar $R3$ structure. There is no nonmagnetic isostructural system that can be used to evaluate the photonic contribution, at least in the current stage.

Nevertheless, the Debye model can be used to fit the $C_p(T)$ data between 80 and 120 K and extrapolate to the low-temperature range for Ni_3TeO_6 and $NiCo_2TeO_6$, evidenced by the solid black lines shown in Fig. 3(d) and Fig. 3(e), respectively. Here, the Debye temperature (Θ_D), which separates the collective motion of ions from the individual motions, is determined to be ~ 429 K for Ni_3TeO_6 and ~ 430 K for $NiCo_2TeO_6$, a typical feature for a compound with lighter atoms such as O^{2-} and strong interionic bonding. After subtracting the phonon contribution from the heat capacity, the magnetic contribution C_m of the heat capacity in $NiCo_2TeO_6$ and Ni_3TeO_6 can be obtained, shown in Figs. 3(d) and 3(e). One sees clearly an enhancement of C_m occurring at T_N, indicating magnetic contribution to the heat capacity. Subsequently, the magnetic entropy $S_m = \int C_m/T\ dT$ for $NiCo_2TeO_6$ and Ni_3TeO_6, can be evaluated and is presented in Fig. 3(f). It is shown that the term S_m for Ni_3TeO_6 reaches up to 21.3 J mol^{-1} K^{-1} at $T_N = 54$ K and saturates near 90 K with a value of 26.9 J mol^{-1} K^{-1}, in good agreement with theoretically predicted values of 27.4 J mol^{-1} K^{-1}. Therefore, the evaluation of phonon contribution using the Debye model works well for Ni_3TeO_6. In contrast, $NiCo_2TeO_6$ retains $S_m = 22.8$ J mol^{-1} K^{-1} between 10 and 90 K, smaller than the predicted value of 32.2 J mol^{-1} K^{-1}, noting that such phenomenon was also observed in polar magnet $Ni_2Mo_3O_8$ [39].

The H dependence of magnetization M for Ni_2CoTeO_6 and $NiCo_2TeO_6$ in the $H//ab$ geometry at several values of T are plotted in Figs. 4(a) and 4(b), respectively, while the $M(H)$ curves for Ni_3TeO_6 in the $H//c$ geometry are shown in Fig. 5(c). In contrast to the nonhysteresis spin-flop transition in Ni_3TeO_6, both Ni_2CoTeO_6 and $NiCo_2TeO_6$ exhibit the H-induced metamagnetic transition with an evident hysteresis loop, characterized by the sudden changes in magnetization. However, the critical magnetic field H_c in the $M(H)$ curve at $T \sim 5$ K is approximately 7.5 T for Ni_2CoTeO_6, quite similar to that of Ni_3TeO_6, while for $NiCo_2TeO_6$ this critical field is dramatically reduced to 2.0 T. As the two compounds exhibit

TABLE II. The effective magnetic moment μ_{eff} and Curie-Weiss temperature θ_{CW} of Ni_2CoTeO_6 and $NiCo_2TeO_6$ for $H//c$ and $H//ab$ were obtained by the Curie-Weiss law fitting above 100 K, μ_{cal} is the calculated effective magnetic moment with $\mu_{Ni}^{2+} = 2.83\ \mu_B$ and $\mu_{Co}^{2+} = 3.87\ \mu_B$, and f_c is the frustration factor along the c axis.

	μ_{eff}^{ab} (μ_B/f.u.)	μ_{eff}^{c} (μ_B/f.u.)	μ_{cal} (μ_B/f.u.)	θ_{CW}^{ab} (K)	θ_{CW}^{c} (K)	f_c
Ni_2CoTeO_6	7.1	7.9	5.6	−27.3	−169.6	3.1
$NiCo_2TeO_6$	12.6	8.9	6.2	−21.4	−214.6	4.4

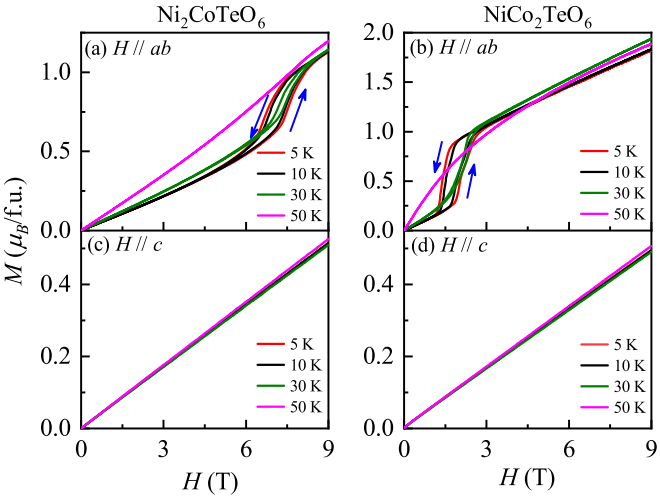

FIG. 4. Magnetic field dependence of magnetization $M(H)$ at various temperatures with $H//ab$ for (a) Ni_2CoTeO_6 and (b) $NiCo_2TeO_6$, and with $H//c$ for (c) Ni_2CoTeO_6 and (d) $NiCo_2TeO_6$, respectively. Arrows indicate measuring cycle.

similar incommensurate AFM helical structure, characterized by ferromagnetic *ab* layers rotating along the *c* axis, the helix periodicity increases with increasing Co^{2+} content [22]. Hence, the reduced H_c is ascribed to the weak anisotropy in the *ab* plane and weak magnetic frustration along the *c* axis. The linear extrapolation of the $M(H)$ data between $H \sim 4.0$ and 9.0 T gives a finite intercept (0.64 μ_B/f.u. at $T \sim 30$ K for $NiCo_2TeO_6$) at $H = 0$, suggesting a spontaneous magnetization component appearing in the *ab* plane above 4 T. Here, "f.u." stands for "formula unit."

As the spins are almost constrained in the *ab* plane, a typical AFM response with weak T dependence is observed in the $H//c$ geometry, as shown in Figs. 4(c) and 4(d). Note that the critical field obtained from our single-crystal data is smaller than the previously reported value [22], and such a difference may be ascribed to the nature of crystals grown by

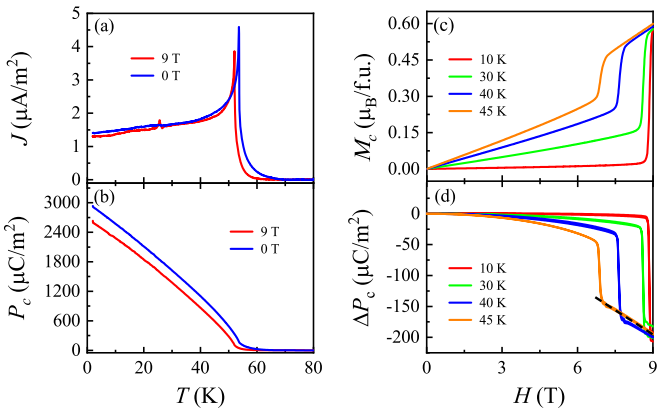

FIG. 5. Temperature dependence of (a) pyroelectric current $J(T)$ and (b) electric polarization along the *c* axis for Ni_3TeO_6 under different H applied along *c* axis. H dependence of (c) magnetization and (d) electric polarization ΔP_c measured at different temperatures under $H//c$. Black dashed line in (d) as guide to the eye indicates linear relationship above H_c.

different methods. In addition, Skiadopoulou *et al.* demonstrated the metamagnetic transition as a spin-flop transition [22]. However, bearing in mind that there is no evident magnetic anisotropy in the helical structure, one cannot expect a spin-flop transition to occur under the magnetic field perpendicular to the helical axis. Thus, neutron-scattering experiments under a magnetic field are required to determine the nature of such metamagnetic transition, which is beyond the scope of this work and unfortunately not accessible at this moment.

C. Magnetoelectric coupling

Before presenting the ME data of Ni_2CoTeO_6 and $NiCo_2TeO_6$, for purpose of comparison, the T-dependent pyroelectric current J and electric polarization P_c of Ni_3TeO_6 under different magnetic fields $H = 0$ and 9 T applied along the *c* axis are presented in Figs. 5(a) and 5(b). Consistent with earlier report [17], a sharp pyroelectric current peak appears at $T_N = 54$ K in the absence of a magnetic field, indicating a large change in the electric polarization. By integrating the pyroelectric current with respect to time, electric polarizations as large as 2920 and 2684 μC/m^2 at $T = 2$ K for $H = 0$ T and $H = 9$ T are obtained, respectively, slightly smaller than the value of 3280 μC/m^2 at $H = 0$ T reported in Ref. [17]. In addition, the H-dependent polarization measurements along the *c* axis were performed in an H-sweeping mode along the *c* axis; see Fig. 5(d). Concomitant with the H-induced metamagnetic transitions as shown in Fig. 5(c), the change of the *c*-axis polarization, i.e., ΔP_c, shows similar nonhysteresis behavior, quite consistent with the data shown in Ref. [17]. By fitting the linear part of $\Delta P_c(H)$ above H_c, the linear ME coefficient $\alpha = 36$ ps/m was obtained at 45 K.

Intrigued by the large ME effect in Ni_3TeO_6, we paid much more attention to the electric polarization (P_c) of Ni_2CoTeO_6 and $NiCo_2TeO_6$ along the *c* axis under the $H//c$ and $H//ab$ configurations. The T-dependent pyroelectric current density (J) for Ni_2CoTeO_6 and $NiCo_2TeO_6$ in the $H//c$-axis geometry, respectively, are is plotted in Figs. 6(a) and 6(b). Similar to Ni_3TeO_6, both compounds show sharp peaks at the magnetic transition points, implying a large change of electric polarization induced by the magnetic ordering. However, the pyroelectric current is somehow H independent, as the magnetic moments are lying in the *ab* plane, and the robust AFM feature is reserved in the case of $H//c$. The electric polarization for Ni_2CoTeO_6 and $NiCo_2TeO_6$ as a function of T at several selected values of H along the *c* axis is displayed in Figs. 6(c) and 6(d), respectively. For Ni_2CoTeO_6, the magnetically induced polarization P_c reaches ~ 340 μC/m^2 under $H = 0$ at $T \sim 2$ K, while it is drastically enhanced up to ~ 2600 μC/m^2 in $NiCo_2TeO_6$, indicating large tunability of the electric polarization by chemical substitution.

In contrast, the situation becomes quite different if one checks the response of polarization P_c to the magnetic field perpendicular to the *c* axis (in the *ab* plane). Figures 7(a) and 7(b) present the pyroelectric current peaks shifting dramatically toward lower T with increasing H, while the intensity of current J below T_N is greatly enhanced. This is quite different from pure Ni_3TeO_6, in which the pyroelectric current is much less sensitive to H, and P_c is suppressed

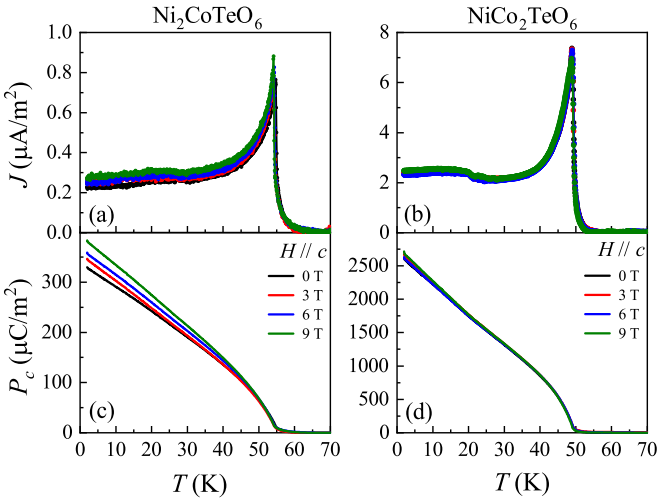

FIG. 6. T dependence of pyroelectric current $J(T)$ for (a) Ni_2CoTeO_6 and (b) $NiCo_2TeO_6$ measured under different H applied along c axis. Corresponding electric polarization along c axis $P_c(T)$ is presented in (c) and (d), respectively.

by H as shown in Fig. 5(b). For the two Co-substituted compounds, a giant P_c up to 5200 $\mu C/m^2$ is achieved for $NiCo_2TeO_6$ at $T \sim 2$ K and $H = 6$ T, in stark contrast to the value of 550 $\mu C/m^2$ for Ni_2CoTeO_6, as shown in Figs. 7(c) and 7(d). Note that for $NiCo_2TeO_6$, the obtained value is larger than most multiferroics and magnetoelectrics, like the time-honored $Fe_2Mo_3O_8$ (3000 $\mu C/m^2$) [16], $Mn_2Mo_3O_8$ (2000 $\mu C/m^2$) [40], and Ni_3TeO_6 (2920 $\mu C/m^2$, this work). This result highlights the remarkable impact of the chemical doping on the ME effect by modulating the magnetic structure of Ni_3TeO_6.

To further investigate the ME effects in Ni_2CoTeO_6 and $NiCo_2TeO_6$, we performed comprehensive H-dependent polarization measurements along the c axis in the H-sweeping mode along and perpendicular to the c axis, respectively.

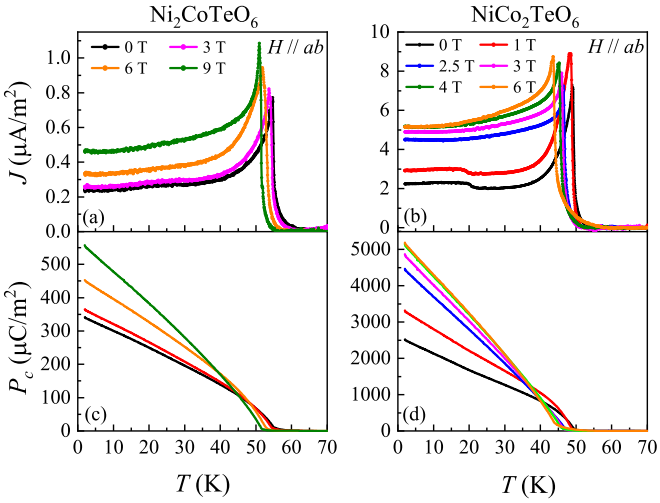

FIG. 7. Temperature dependence of pyroelectric current $J(T)$ for (a) Ni_2CoTeO_6 and (b) $NiCo_2TeO_6$ measured with different H applied normal to c axis. Corresponding electric polarization along c axis $P_c(T)$ is presented in (c) and (d), respectively.

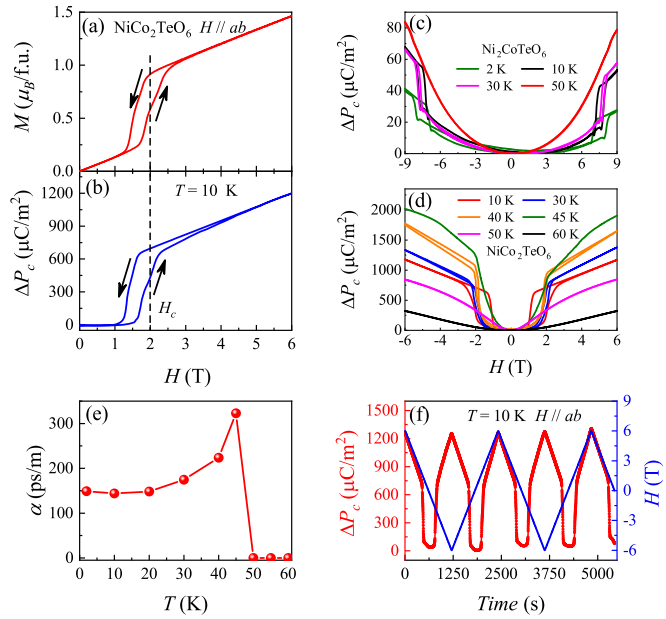

FIG. 8. H-dependent (a) magnetization and (b) magnetically driven polarization ΔP_c of $NiCo_2TeO_6$ at 10 K for H applied along ab plane. H-dependent ΔP_c under various temperatures with H parallel to ab plane for (c) Ni_2CoTeO_6 and (d) $NiCo_2TeO_6$. (e) T-dependent ME coupling coefficients α of $NiCo_2TeO_6$ in field-up run. (f) Modulated electric polarization as a function of time with respect to linearly varying magnetic field (blue color) between −6 and 6 T along ab plane at 10 K.

Concomitant with the H-induced metamagnetic transitions, the change of the c-axis polarization ΔP_c shows similar hysteresis behavior well identified near $H \sim H_c$ for $NiCo_2TeO_6$ at $T = 10$ K; see Figs. 8(a) and 8(b). In detail, the $\Delta P_c(H)$ curve shows a rapid rise as H is larger than 1.0 T. Then, with further increasing H, a linear behavior with the one-to-one correspondences between $\Delta P_c(H)$ and $M(H)$ is observed, indicative of intrinsic magnetically induced polarization. Different from the collinear spin ordering in Ni_3TeO_6, the ground state here is an incommensurate AFM helical structure; thus, a relatively broad intermediate state is initiated at the metamagnetic transition, giving rise to the distinct hysteresis behavior in $\Delta P_c(H)$ and $M(H)$.

In Figs. 8(c) and 8(d), we present more detailed data on the H-dependent ΔP_c measured at various T for Ni_2CoTeO_6 and $NiCo_2TeO_6$, respectively. The most striking result is the tremendous enhancement of the ME response. For instance, a change of ΔP_c up to 2000 $\mu C/m^2$ at $T \sim 45$ K is achieved, almost 10 times larger than the value of 201 $\mu C/m^2$ at $T \sim 10$ K for Ni_3TeO_6. No significant ME effect can be observed for the change of ΔP_c in response to magnetic field applied parallel to the c axis.

In order to evaluate the ME coupling, the linear ME susceptibility α, defined by $\alpha = P/H$, is evaluated by the linear fitting to the $\Delta P_c(H)$ curve in the magnetic field ranges 3 T $< H <$ 6 T below $T = 40$ K and 3 T $< H <$ 4 T for $T = 45$ K in the field-up run. The T-dependent α data for $NiCo_2TeO_6$ are summarized in Fig. 8(e), which show considerably strong coupling up to 323 ps/m at $T \sim 45$ K,

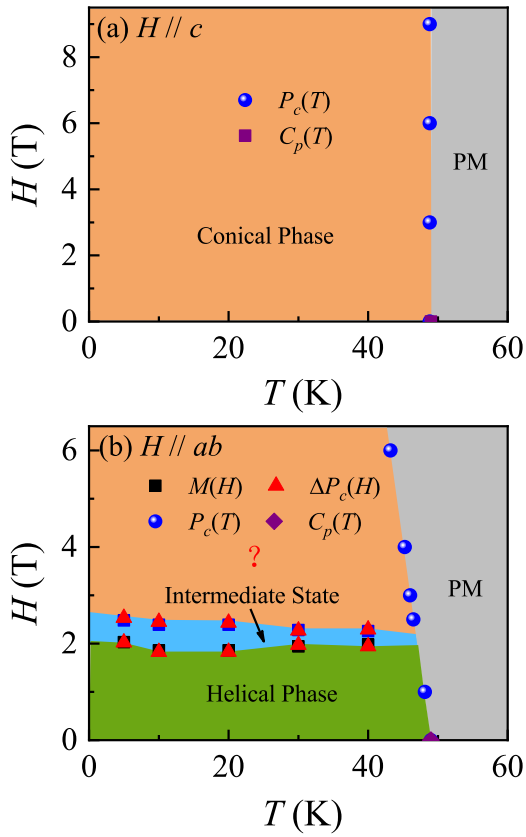

FIG. 9. (a) H-T phase diagrams of $NiCo_2TeO_6$ with magnetic field applied along c axis and (b) ab plane.

much larger than those typically linear ME effects in Cr_2O_3 ($\alpha \sim 4.13$ ps/m) [41], $Fe_2Mo_3O_8$ ($\alpha \sim 16.2$ ps/m) [27], $Ni_2Mo_3O_8$ ($\alpha \sim 70$ ps/m) [42], and Sm_2BaCuO_5 ($\alpha \sim 4.4$ ps/m) [43]. For the case of Ni_2CoTeO_6, the linear ME coefficient α is only 3.4 ps/m at $T \sim 45$ K, much smaller than those of Ni_3TeO_6 and $NiCo_2TeO_6$.

Another distinct feature is that the largest ME effect dominates in the T window just below T_N, whereas the electric polarization and ME coefficient reach their maxima at the lowest temperature for Ni_3TeO_6. Such a large ME response seems to be unusual, and we argue that the exchange interaction and magnetostriction are responsible for the variation of polarization, which will be discussed in detail later. In addition, we depict the variation of ΔP_c induced by a modulated magnetic field along the ab plane at $T \sim 10$ K, with periodic variation between 6 and -6 T, as shown in Fig. 8(f).

D. Magnetic phase diagram

Based on the experimental results obtained from the magnetization, pyroelectric current, electric polarization, and heat capacity, the ME phase diagrams in the (H, T) space for $H//c$ and $H//ab$ planes are developed for $NiCo_2TeO_6$ in the field-up runs; see Figs. 9(a) and 9(b). We find three magnetic phases: helical phase, intermediate state, and the unclear phase denoted as "?", separated by the corresponding phase boundaries. In Fig. S5 we present the $(dM_{ab}/dH) - H$ and $(dP/dH) - H$ curves at several selected values of T in the field-up run, respectively, while the $(dM_{ab}/dH) - H$ and $(dP/dH) - H$ curves in the field-down run are also shown [32]. To determine the phase-transition points of the "intermediate state" in the field-up (field-down) runs, the starting (ending) point of the intermediate state is located at the lower H peak of the $(dP/dH) - H$ curve (denoted as H_{c1}) while the position of the right peak in the $(dM_{ab}/dH) - H$ curve is designed as the ending (starting) point of the intermediate state (denoted as H_{c2}). From this point of view, the phase-transition points of the intermediate state determined by the method are not an internal state but represent the start and end of the intermediate state. The consistency between the phase boundaries defined by M and ΔP_c indicates a strong intercorrelation between magnetism and electricity. In contrast, for the $H//c$ axis, only a conical magnetic phase is dominated in the low-field region.

E. Discussion

Given the aforementioned large-tunability ME coupling in Ni_2CoTeO_6 and $NiCo_2TeO_6$, a tentative discussion on the microscopic mechanism of ME coupling effects becomes appreciated. Up to now, the magnetically induced electric polarization can be explained by three well-known mechanisms: (1) spin current or inverse Dzyaloshinskii-Moriya (DM) mechanism [44], (2) metal-ligand p–d hybridization mechanism [45], and (3) symmetric exchange striction mechanism [46]. The spin current or inverse DM mechanism cannot work effectively in this system due to the proper-screw helicoid magnetic structure. The changes in the electric polarization induced by the metal-ligand p–d hybridization mechanism ΔP_c can be expressed as $\Delta P_c \propto C_1 S^2 \sin^2\theta + C_2 S^2 \cos^2\theta = C_1 S^2 + (C_2 - C_1) S_z^2$ [47], where C_1 and C_2 are the coupling constants correlated to the structural parameters of NiO6 octahedra, S is the magnetic moment, and S_z is the z component of the moment. Since the spins mainly lie in the ab plane, ΔP_c should be a constant, in contradiction with the linear response of ΔP_c to the magnetic field for $H > H_c$. Taking all these into account, the symmetry exchange-striction mechanism should govern the ME response in $Ni_{3-x}Co_xTeO_6$ through the modulation of exchange interactions, similar to the case of Ni_3TeO_6.

However, there is also a significant difference between Ni_3TeO_6 and the Co^{2+}-doped samples, in which ΔP_c and ME coefficients α, as shown in Figs. 8(d) and 8(e), approach their maximum values near T_N, in stark contrast to Ni_3TeO_6, where the ME coefficient exhibits the strongest values at low T. Actually, such phenomena were also observed in the compound $CaBaCo_4O_7$ [14]. The large change in electric polarization and enhanced ME coefficient are attributed to the giant magnetostriction caused by the Co^{2+} ions [48]. Since the spin-orbital coupling is also significant in the Co^{2+}-doping compounds, it is argued that the magnetostriction in $Ni_{3-x}Co_xTeO_6$ may also play an important role (to be discussed briefly here), while the Heisenberg exchange striction still works, similar to the case of Ni_3TeO_6.

In Ni_3TeO_6, the Ni ions at Ni1 and Ni2 sites have inequivalent environments with different elasticities and their charges may be slightly different, forming a dipole along the c axis in Ni1-O6/Ni2-O6 dimer. In the magnetically ordered

state, the symmetric Heisenberg exchange striction between the magnetic ions at Ni1 and Ni2 sites will change the bond lengths in NiO6 octahedra, as reported in recent work [49], and subsequently the distorted NiO6 octahedra distortion, in turn, modifies the electric polarization. In the case of Ni_3TeO_6, accompanied by the spin-flop transition, the spins at Ni1 and Ni2 sites rotate rapidly from the c axis to the in plane, leading to the large change in electric polarization and colossal ME effect. In contrast, as the unquenched orbital angular momentum in $Ni_{3-x}Co_xTeO_6$ couples with spin momentum and tetragonal distortion of the octahedral crystal field, the O^{2-} ions in Ni1-O6 and Ni2-O6 octahedra shift their positions through magnetoelastic coupling, namely the Joule magnetostriction, in response to the rotation of the magnetic moments under the magnetic field applied along the *ab* plane. The shifts of O^{2-} ions can change the bond length and thus alter the polarization compared with the paramagnetic state.

More importantly, earlier works on the magneto-infrared responses [20,49], high-field optical spectroscopy [50], and theoretical calculation [51] have shown that the magnetic interaction between Ni1 and Ni2 in Ni_3TeO_6 plays a dominant role in magnetic properties, electronic structure, and magnetic-induced electric polarization. In the case of Ni_2CoTeO_6, the Ni ions at Ni1 and Ni2 sites are partially substituted by the Co^{2+} ions, and the distortion of the polar crystal structure, which is induced by the magnetostriction, should be largely alleviated, giving rise to the greatly destroyed magnetically induced electric polarization and ME coupling effects. On the contrary, with increasing Co^{2+} content, the Ni2 sites are fully occupied by the Co^{2+} ions in $NiCo_2TeO_6$, as presented in Table I, indicating magnetostriction plays an increasingly important role here, thus giving rise to a larger distortion of the polar crystal structure, concomitant with the significantly enhanced ME coupling effects.

Chubokov *et al.* [52], however, demonstrated that the magnetic moments of a hexagonal antiferromagnet would be confined in plane if its in-plane anisotropy parameter D was of the same order of magnitude or even greater than the exchange interaction in the basal plane, even though a strong magnetic field is applied along out of plane. This effect, that the in-plane single-ion anisotropy is much stronger than the dominant exchange interaction, is usually found in cobaltites, such as $Co_4Nb_2O_9$ [53] and $Ba_2CoGe_2O_7$ [54]. Along this line, it is reasonably expected in $Ni_{3-x}Co_xTeO_6$, whereas the in-plane magnetic order can be easily affected by the external magnetic field more than the antiferromagnetic stack along the c axis. Therefore, either M_{ab} or ME coupling is significantly larger than that of the c axis. When H is applied along the c axis, the magnetic structures should be conical with the coning angle close to 90 °; thus, M_c should increase linearly with the magnetic field and finally saturate at an ultrahigh magnetic field.

IV. CONCLUSION

In summary, we have systematically investigated the Co^{2+} doping-induced consequences in terms of the crystal structure, magnetic property, and ME coupling in polar antiferromagnets $Ni_{3-x}Co_xTeO_6$ ($x = 1, 2$) single crystals. Our results have revealed that the linear ME coefficient α upon the Co^{2+} substitution can be remarkably modulated, evidenced by the high $\alpha \sim 326$ ps/m for $NiCo_2TeO_6$, small $\alpha \sim 3.4$ ps/m for Ni_2CoTeO_6, and intermediate $\alpha \sim 36$ ps/m for Ni_3TeO_6 at temperature $T \sim 45$ K. The large-tunability ME properties are believed to be associated with the different occupations of the Ni/Co ions at the specific lattice sites. In the case of Ni_2CoTeO_6, the Ni ions at Ni1 and Ni2 sites are partially substituted by the Co^{2+} ions, and the distortion of the polar crystal structure which is induced by the magnetostriction should be largely alleviated, giving rise to the greatly destroyed magnetically induced electric polarization and ME coupling effects. On the contrary, with increasing Co content, the Ni2 sites are fully occupied by the Co^{2+} ions in $NiCo_2TeO_6$, indicating magnetostriction plays an increasingly important role here. Hence, the magnetostriction and Heisenberg exchange striction both play important roles in the modulation of ME effects. Our work provides insights into designing the significant ME coupling properties in Ni_3TeO_6-type polar magnets.

ACKNOWLEDGMENT

The authors would like to acknowledge the financial support from the National Natural Science Foundation of China (Grants No. 92163210, No. 12274231, No. 11834002, No. 12074111, No. 51721001, No. 52272108, and No. 11974167).

[1] S.-W. Cheong and M. Mostovoy, Multiferroics: A magnetic twist for ferroelectricity, Nat. Mater. **6**, 13 (2007).

[2] S. Dong, J.-M. Liu, S.-W. Cheong, and Z. F. Ren, Multiferroic materials and magnetoelectric physics: Symmetry, entanglement, excitation, and topology, Adv. Phys. **64**, 519 (2015).

[3] Y. Tokura, S. Seki, and N. Nagaosa, Multiferroics of spin origin, Rep. Prog. Phys. **77**, 076501 (2014).

[4] N. A. Spaldin and R. Ramesh, Advances in magnetoelectric multiferroics, Nat. Mater. **18**, 203 (2019).

[5] S. Reschke, D. G. Farkas, A. Strinić, S. Ghara, K. Guratinder, O. Zaharko, L. Prodan, V. Tsurkan, D. Szaller, S. Bordács, J. Deisenhofer, and I. Kézsmárki, Confirming the trilinear form of the optical magnetoelectric effect in the polar honeycomb antiferromagnet $Co_2Mo_3O_8$, npj Quantum Mater. **7**, 1 (2022).

[6] N. D. Khanh, N. Abe, H. Sagayama, A. Nakao, T. Hanashima, R. Kiyanagi, Y. Tokunaga, and T. Arima, Magnetoelectric coupling in the honeycomb antiferromagnet $Co_4Nb_2O_9$, Phys. Rev. B **93**, 075117 (2016).

[7] I. Kornev, M. Bichurin, J.-P. Rivera, S. Gentil, H. Schmid, A. G. M. Jansen, and P. Wyder, Magnetoelectric properties of $LiCoPO_4$ and $LiNiPO_4$, Phys. Rev. B **62**, 12247 (2000).

[8] K. Kimura, Y. Kato, S. Kimura, Y. Motome, and T. Kimura, Crystal-chirality-dependent control of magnetic domains in a time-reversal-broken antiferromagnet, npj Quantum Mater. **6**, 54 (2021).

[9] C. De, R. Bag, S. Singh, O. Fabelo, M. T. Fernández-Díaz, N. V. Ter-Oganessian, and A. Sundaresan, Magnetoelectric effect

in a single crystal of the frustrated spinel $CoAl_2O_4$, Phys. Rev. B **103**, 094406 (2021).

[10] S. Mishra, P. Yanda, and A. Sundaresan, Magnetoelectric effect in the honeycomb-lattice antiferromagnet $BaNi_2(PO_4)_2$, Phys. Rev. B **103**, 214443 (2021).

[11] S.-W. Cheong and X. Xu, Magnetic chirality, npj Quantum Mater. **7**, 40 (2022).

[12] T. Kimura, Y. Sekio, H. Nakamura, T. Siegrist, and A. P. Ramirez, Cupric oxide as an induced-multiferroic with high-T_C, Nat. Mater. **7**, 291 (2008).

[13] F. Damay, J. Sottmann, F. Fauth, E. Suard, A. Maignan, and C. Martin, High temperature spin-driven multiferroicity in ludwigite chromocuprate Cu_2CrBO_5, Appl. Phys. Lett. **118**, 192903 (2021).

[14] V. Caignaert, A. Maignan, K. Singh, Ch. Simon, V. Pralong, B. Raveau, J. F. Mitchell, H. Zheng, A. Huq, and L. C. Chapon, Gigantic magnetic-field-induced polarization and magnetoelectric coupling in a ferrimagnetic oxide $CaBaCo_4O_7$, Phys. Rev. B **88**, 174403 (2013).

[15] V. Kocsis, Y. Tokunaga, S. Bordács, M. Kriener, A. Puri, U. Zeitler, Y. Taguchi, Y. Tokura, and I. Kézsmárki, Magnetoelectric effect and magnetic phase diagram of a polar ferrimagnet $CaBaFe_4O_7$, Phys. Rev. B **93**, 014444 (2016).

[16] Y. Wang, G. L. Pascut, B. Gao, T. A. Tyson, K. Haule, V. Kiryukhin, and S.-W. Cheong, Unveiling hidden ferrimagnetism and giant magnetoelectricity in polar magnet $Fe_2Mo_3O_8$, Sci. Rep. **5**, 12268 (2015).

[17] Y. S. Oh, S. Artyukhin, J. J. Yang, V. Zapf, J. W. Kim, D. Vanderbilt, and S.-W. Cheong, Non-hysteretic colossal magnetoelectricity in a collinear antiferromagnet, Nat. Commun. **5**, 3201 (2014).

[18] K. Momma and F. Izumi, VESTA 3 for three-dimensional visualization of crystal, volumetric and morphology data, J. Appl. Crystallogr. **44**, 1272 (2011).

[19] J. W. Kim, S. Artyukhin, E. D. Mun, M. Jaime, N. Harrison, A. Hansen, J. J. Yang, Y. S. Oh, D. Vanderbilt, V. S. Zapf, and S.-W. Cheong, Successive Magnetic-field-induced Transitions and Colossal Magnetoelectric Effect in Ni_3TeO_6, Phys. Rev. Lett **115**, 137201 (2015).

[20] M. O. Yokosuk, A. al-Wahish, S. Artyukhin, K. R. O'Neal, D. Mazumdar, P. Chen, J. Yang, Y. S. Oh, S. A. McGill, K. Haule, S.-W. Cheong, D. Vanderbilt, and J. L. Musfeldt, Magnetoelectric Coupling through the Spin-Flop Transition in Ni_3TeO_6, Phys. Rev. Lett. **117**, 147402 (2016).

[21] J. Kim, J. Yang, C. J. Won, K. Kim, B. Kim, D. Obeysekera, D. W. Lee, and S.-W. Cheong, Helical versus collinear antiferromagnetic order tuned by magnetic anisotropy in polar and chiral $(Ni, Mn)_3TeO_6$, Phys. Rev. Mater. **5**, 094405 (2021).

[22] S. Skiadopoulou, M. Retuerto, F. Borodavka, C. Kadlec, F. Kadlec, M. Míšek, J. Prokleška, Z. Deng, X. Y. Tan, C. Frank, J. A. Alonso, M. T. Fernandez-Diaz, M. Croft, F. Orlandi, P. Manuel, E. McCabe, D. Legut, M. Greenblatt, and S. Kamba, Structural, magnetic, and spin dynamical properties of the polar antiferromagnets $Ni_{3-x}Co_xTeO_6$ ($x = 1,\ 2$), Phys. Rev. B **101**, 014429 (2020).

[23] C. W. Wang, C. H. Lee, C. Y. Li, C. M. Wu, W. H. Li, C. C. Chou, H. D. Yang, J. W. Lynn, Q. Z. Huang, A. B. Harris, and H. Berger, Complex magnetic coupling in Co_3TeO_6, Phys. Rev. B **88**, 184427 (2013).

[24] M. Hudl, R. Mathieu, S. A. Ivanov, M. Weil, V. Carolus, T. Lottermoser, M. Fiebig, Y. Tokunaga, Y. Taguchi, Y. Tokura, and P. Nordblad, Complex magnetism and magnetic-field-driven electric polarization of Co_3TeO_6, Phys. Rev. B **84**, 180404(R) (2011).

[25] A. Bhim, J. Gopolakrishnan, and S. Natarajan, Exploring the corundum structure as a host for colored compounds-synthesis, structures, and optical studies of $(MM')_3TeO_6$ (M = Mg, Mn, Co, Ni, Zn; M′ = Mg, Mn, Co, Ni, Cu), Eur. J. Inorg. Chem. **2018**, 2277 (2018).

[26] R. P. Chaudhury, F. Ye, J. A. Fernandez-Baca, B. Lorenz, Y. Q. Wang, Y. Y. Sun, H. A. Mook, and C. W. Chu, Robust ferroelectric state in multiferroic $Mn_{1-x}Zn_xWO_4$, Phys. Rev. B **83**, 014401 (2011).

[27] T. Kurumaji, S. Ishiwata, and Y. Tokura, Doping-Tunable Ferrimagnetic Phase with Large Linear Magnetoelectric Effect in A Polar Magnet $Fe_2Mo_3O_8$, Phys. Rev. X **5**, 031034 (2015).

[28] S. Seki, Y. Yamasaki, Y. Shiomi, S. Iguchi, Y. Onose, and Y. Tokura, Impurity-doping-induced ferroelectricity in the frustrated antiferromagnet $CuFeO_2$, Phys. Rev. B **75**, 100403(R) (2007).

[29] Y. Tokunaga, Y. Kaneko, D. Okuyama, S. Ishiwata, T. Arima, S. Wakimoto, K. Kakurai, Y. Taguchi, and Y. Tokura, Multiferroic M-type Hexaferrites with a Room-Temperature Conical State and Magnetically Controllable Spin Helicity, Phys. Rev. Lett. **105**, 257201 (2010).

[30] B. H. Toby, EXPGUI, a graphical user interface for GSAS, J. Appl. Crystallogr. **34**, 210 (2001).

[31] L. Lin, Y. S. Tang, L. Huang, W. J. Zhai, G. Z. Zhou, J. H. Zhang, M. F. Liu, G. Y. Li, X. Y. Li, Z. B. Yan, and J. -M. Liu, Observation of magnetoelectric effect in the $S = 1/2$ spin chain compound $CoSe_2O_5$ single crystal, Appl. Phys. Lett. **120**, 052901 (2022).

[32] See Supplemental Material at http://link.aps.org/supplemental/10.1103/PhysRevB.108.024107 for Laue diffraction spots and Rietveld refinement of Ni_3TeO_6, the EDX mapping images of the Ni, Co, Te, and O elements for Ni_2CoTeO_6 and $NiCo_2TeO_6$, the $(dM_{ab}/dH) - H$ and $(dP/dH) - H$ curves for $NiCo_2TeO_6$.

[33] H. Schulz and G. Bayer, Structure determination of Mg_3TeO_6, Acta Crystallogr. Sect. B **27**, 815 (1971).

[34] M. Weil, Mn_3TeO_6, Acta Crystallogr. Sect. E **62**, i244 (2006).

[35] M. Weil, Zn_3TeO_6, Acta Crystallogr. Sect. E **62**, i246 (2006).

[36] S. A. Ivanov, R. Tellgren, C. Ritter, P. Nordblad, R. Mathieu, G. Andre, N. V. Golubko, E. D. Politova, and M. Weil, Temperature-dependent multi-k magnetic structure in multiferroic Co_3TeO_6, Mater. Res. Bull. **47**, 63 (2012).

[37] M. Herak, H. Berger, M. Prester, M. Miljak, I. Živković, O. Milat, D. Drobac, S. Popović, and O. Zaharko, Novel spin lattice in Cu_3TeO_6: An antiferromagnetic order and domain dynamics, J. Phys.: Condens. Matter **17**, 7667 (2005).

[38] R. Becker and H. Berger, Reinvestigation of Ni_3TeO_6, Acta Crystallogr. Sect. E **62**, i222 (2006).

[39] J. R. Morey, A. Scheie, J. P. Sheckelton, C. M. Brown, and T. M. McQueen, $Ni_2Mo_3O_8$: Complex antiferromagnetic order on a honeycomb lattice, Phys. Rev. Mater. **3**, 014410 (2019).

[40] T. Kurumaji, S. Ishiwata, and Y. Tokura, Diagonal magnetoelectric susceptibility and effect of Fe doping in the polar ferrimagnet $Mn_2Mo_3O_8$, Phys. Rev. B **95**, 045142 (2017).

[41] H. Wiegelmann, A. G. M. Jansen, P. Wyder, J.-P. Rivera, and H. Schmid, Magnetoelectric effect of Cr_2O_3 in strong static magnetic fields, Ferroelectrics **162**, 141 (1994).

[42] Y. S. Tang, J. H. Zhang, L. Lin, R. Chen, J. F. Wang, S. H. Zheng, C. Li, Y. Y. Zhang, G. Z. Zhou, L. Huang, Z. B. Yan, X. M. Lu, D. Wu, X. K. Huang, X. P. Jiang, and J.-M. Liu, Metamagnetic transitions and magnetoelectricity in the spin-1 honeycomb antiferromagnet $Ni_2Mo_3O_8$, Phys. Rev. B **103**, 014112 (2021).

[43] G. Z. Zhou, J. W. Gong, X. Li, M. F. Liu, L. Y. Li, Y. Wang, J. H. Min, J. Liu, D. Cai, F. Liu, S. H. Zheng, Y. S. Tang, Z. C. Xu, Y. L. Xie, L. Yang, M. Zeng, Z. B. Yan, B. W. Li, X. Z. Wang, and J.-M. Liu, Large magnetoelectric effect in the polar magnet Sm_2BaCuO_5, Appl. Phys. Lett. **115**, 252902 (2019).

[44] H. Katsura, N. Nagaosa, and A. V. Balatsky, Spin Current and Magnetoelectric Effect in Noncollinear Magnets, Phys. Rev. Lett. **95**, 057205 (2005).

[45] T. Arima, Ferroelectricity induced by proper-screw type magnetic order, J. Phys. Soc. Jpn. **76**, 073702 (2007).

[46] I. A. Sergienko, C. Şen, and E. Dagotto, Ferroelectricity in the Magnetic *E*-Phase of Orthorhombic Perovskites, Phys. Rev. Lett. **97**, 227204 (2006).

[47] J. H. Zhang, Y. S. Tang, L. Lin, L. Y. Li, G. Z. Zhou, B. Yang, L. Huang, X. Y. Li, G. Y. Li, S. H. Zheng, M. F. Liu, M. Zeng, D. Wu, Z. B. Yan, X. K. Huang, C. Chen, X. P. Jiang, and J.-M. Liu, Electric polarization reversal and nonlinear magnetoelectric coupling in the honeycomb antiferromagnet $Fe_4Nb_2O_9$ single crystal, Phys. Rev. B **107**, 024108 (2023).

[48] Y.-S. Chai, J.-Z. Cong, J.-C. He, D. Su, X.-X. Ding, J. Singleton, V. Zapf, and Y. Sun, Giant magnetostriction and nonsaturating electric polarization up to 60 T in the polar magnet $CaBaCo_4O_7$, Phys. Rev. B **103**, 174433 (2021).

[49] M. O. Yokusuk, S. Artyukhin, A. al-Wahish, X. Y. Wang, J. J. Yang, Z. Q. Li, S.-W. Cheong, D. Vanderbilt, and J. L. Musfeldt, Tracking the continuous spin-flop transition in Ni_3TeO_6 by infrared spectroscopy, Phys. Rev. B **92**, 144305 (2015).

[50] K. Park, M. O. Yokosuk, M. Goryca, J. J. Yang, S. A. Crooker, S. -W. Cheong, K. Haule, D. Vanderbilt, H.-S. Kim, and J. L. Musfeldt, Nonreciprocal directional dichroism at telecom wavelengths, npj Quantum Mater. **7**, 38 (2022).

[51] F. Wu, E. J. Kan, C. Tian, and M.-H. Whangbo, Theoretical analysis of the spin exchange and magnetic dipole-dipole interaction leading to the magnetic structure of Ni_3TeO_6, Inorg. Chem. **49**, 7545 (2010).

[52] A. V. Chubkov, Quasi-one-dimensional hexagonal antiferromagnets in a magnetic field, J. Phys. C: Solid State Phys. **21**, L441 (1988).

[53] G. C. Deng, Y. M. Cao, W. Ren, S. X. Cao, A. J. Studer, N. Gauthier, M. Kenzelmann, G. Davidson, K. C. Rule, J. S. Gardner, P. Imperia, C. Ulrich, and G. J. McIntyre, Spin dynamics and magnetoelectric coupling mechanism of $Co_4Nb_2O_9$, Phys. Rev. B **97**, 085154 (2018).

[54] J. Romhányi and K. Penc, Multiboson spin-wave theory for $Ba_2CoGe_2O_7$: A spin-3/2 easy-plane Néel antiferromagnet with strong single-ion anisotropy, Phys. Rev. B **86**, 174428 (2012).